ORIGINAL ARTICLE



Automated quantification of brain PET in PET/CT using deep learning-based CT-to-MR translation: a feasibility study

Daesung Kim¹ · Kyobin Choo² · Sangwon Lee³ · Seongjin Kang³ · Mijin Yun³ · Jaewon Yang⁴

Received: 7 October 2024 / Accepted: 3 February 2025 / Published online: 18 February 2025 © The Author(s), under exclusive licence to Springer-Verlag GmbH Germany, part of Springer Nature 2025

Abstract

Purpose Quantitative analysis of PET images in brain PET/CT relies on MRI-derived regions of interest (ROIs). However, the pairs of PET/CT and MR images are not always available, and their alignment is challenging if their acquisition times differ considerably. To address these problems, this study proposes a deep learning framework for translating CT of PET/CT to synthetic MR images (MR_{SYN}) and performing automated quantitative regional analysis using MR_{SYN} -derived segmentation. Methods In this retrospective study, 139 subjects who underwent brain [^{18}F]FBB PET/CT and T1-weighted MRI were included. A U-Net-like model was trained to translate CT images to MR_{SYN} ; subsequently, a separate model was trained to segment MR_{SYN} into 95 regions. Regional and composite standardised uptake value ratio (SUVr) was calculated in [^{18}F]FBB PET images using the acquired ROIs. For evaluation of MR_{SYN} , quantitative measurements including structural similarity index measure (SSIM) were employed, while for MR_{SYN} -based segmentation evaluation, Dice similarity coefficient (DSC) was calculated. Wilcoxon signed-rank test was performed for SUVrs computed using MR_{SYN} and ground-truth MR (MR_{GT}). Results Compared to MR_{GT} , the mean SSIM of MR_{SYN} was 0.974 ± 0.005 . The MR_{SYN} -based segmentation achieved a mean DSC of 0.733 across 95 regions. No statistical significance (P > 0.05) was found for SUVr between the ROIs from MR_{SYN} and those from MR_{GT} , excluding the precuneus.

Conclusion We demonstrated a deep learning framework for automated regional brain analysis in PET/CT with MR_{SYN}. Our proposed framework can benefit patients who have difficulties in performing an MRI scan.

 $\textbf{Keywords} \ \ PET/CT \cdot Amyloid \cdot Quantification \cdot Deep \ learning \cdot Segmentation$

Mijin Yun and Jaewon Yang contributed equally to this work.

Daesung Kim and Kyobin Choo contributed equally to this work.

- Mijin Yun yunmijin@yuhs.ac
- Department of Artificial Intelligence, Yonsei University, Seoul, Republic of Korea
- Department of Computer Science, Yonsei University, Seoul, Republic of Korea
- Department of Nuclear Medicine, Yonsei University College of Medicine, Seoul, Republic of Korea
- Department of Radiology, University of Texas Southwestern, Dallas, TX, USA

Introduction

The biological definition of Alzheimer's disease is characterised by the deposition of β -amyloid (A β), pathologic tau proteins, and neurodegeneration [1]. Among these biomarkers, the deposition of A β in cortical gray matter can be observed via PET/CT images with various radiotracers [2]. However, current clinical practice of interpreting amyloid PET/CT images relies on the visual analysis of PET images, which is prone to inter-rater variability [3]. Consequently, active research has focused on machine-assisted quantitative measurement of cortical amyloid load in amyloid PET/CT scans [4, 5].

Various approaches have been suggested for quantifying amyloid load in amyloid PET/CT scans. First, spatial normalization (SN)-based methods register PET images to the standard Montreal Neurological Institute (MNI) space [6–8], which allows measurement of standardised uptake value ratio (SUVr) using predefined regions of interest (ROIs).



However, SN-based methods have limited effectiveness in distinguishing amyloid-positive PET images from negative ones because the ROIs are not designed to specify each patient's gray matter [9]. In contrast, segmentation-based methods can define patient-specific ROIs by segmenting anatomical MR images with software such as FreeSurfer [10, 11], which offers greater power for identifying amyloid-positive PET images [12]; nonetheless, high-quality 3D T1-weighted MR images are not always available for all PET examinees and are vulnerable to susceptibility artifacts and potential registration errors between MRI and PET [13, 14].

Instead, brain CT images could be an alternative to MRI for anatomical segmentation [15]. Currently, brain PET/CT is the standard for brain imaging as PET/MRI devices are not available in most medical centres. While CT has much lower soft-tissue contrast compared to MRI in the brain, CT images have demonstrated the potential for extracting regional information via deep learning (DL), enabling CT-based regional brain analysis in PET [16, 17]. Recently, to overcome the challenge of limited soft-tissue contrast in CT, a multi-task DL model that simultaneously performs CT segmentation and CT-to-MR translation has been proposed for segmenting only gray matter in CT scans [18]. However, previous studies do not segment gray matter into cortical structures comparable to the FreeSurfer ROIs and have not been validated on quantifying PET images.

To address this problem, we aim to develop a DL framework for translating CT of PET/CT to synthetic MR images (MR_{SYN}) and performing automated regional brain analysis in amyloid PET using MR_{SYN} -based segmentation. The pipeline of our automated analysis framework consists of three steps: 1) CT-to-MR translation for MR_{SYN} generation, 2) automatic segmentation of 95 regions in the brain using MR_{SYN} , and 3) SUVr quantification in each ROI. Subsequently, the quality of MR_{SYN} , the accuracy of MR_{SYN} -based

Table 1 Subject demographics

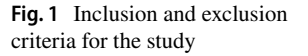
	Train and validation set $(n=99)$	Test set $(n=33)$
Sex	,	
Female	63	20
Male	36	13
Age \pm SD, years	72.1 ± 8.2	70.0 ± 8.7

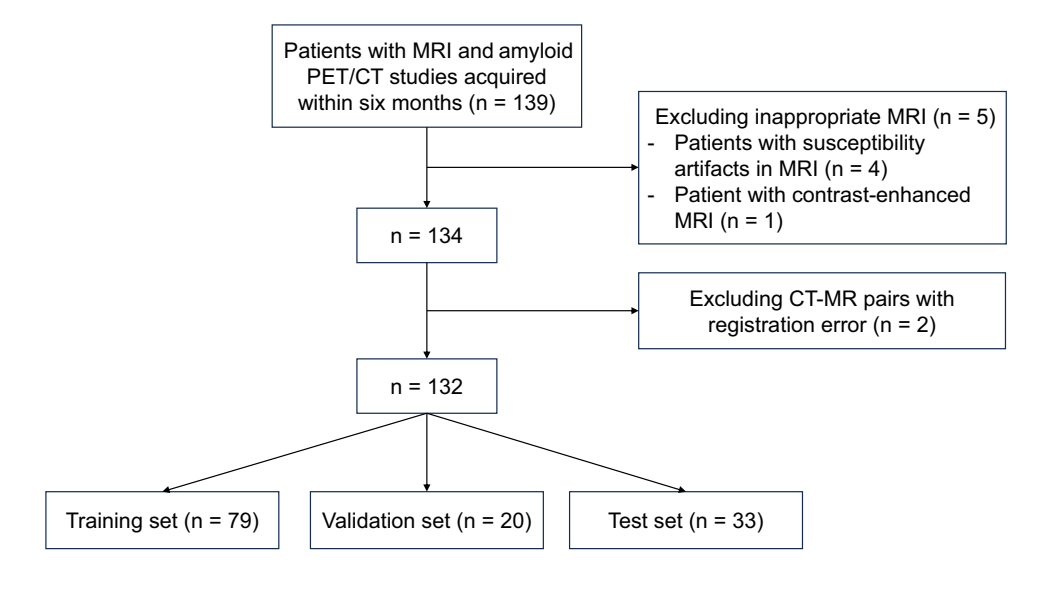
brain segmentation, and the quantitative (i.e., SUVr) agreement between ground truth MR images (MR_{GT})-based analysis and MR_{SYN} -based analysis were evaluated at each step.

Materials and methods

Patients and data description

139 pairs of [¹⁸F]Florbetaben ([¹⁸F]FBB) PET/CT and T1-weighted MRI studies performed between February 2016 and November 2022 were retrospectively collected at the dementia clinic at Severance Hospital. The study received approval from the institutional review board of Severance Hospital, and the need for informed consent was waived given the retrospective nature of the study. All data underwent visual scrutiny with a focus on registration accuracy. Four pairs were excluded from the study due to susceptibility artefacts, 2 due to registration error, and 1 due to disparate MR protocol without 3D T1-weighted MR images. The inclusion–exclusion criteria for the study are illustrated in Fig. 1 The data were split into 79 (60%), 20 (15%), and 33 (25%) pairs for training, validation, and testing. The demographic data for the study dataset are summarised in Table 1.







PET/CT acquisition

[¹⁸F]FBB PET/CT studies were conducted with Discovery 600 (GE Medical Systems, USA). First, [¹⁸F]FBB was intravenously injected into patients at a dose of 300 MBq. PET scanning was performed 90 min after the injection for 20 min in the list mode. The spiral CT scan was performed with a rotation time of 0.8 s at 120 kVp, 200 mA, 3.75 mm slice thickness, 10.0 mm collimation, and 9.375 mm table feed per rotation. Images were reconstructed using the ordered subset expectation maximization algorithm with four iterations and 32 subsets. Reconstructed PET images were then subjected to a Gaussian filter with a full-width at half-maximum (FWHM) of 4 mm. The resulting PET images were in a 256×256 matrix with a pixel size of 0.98 mm and a slice thickness of 3.75 mm.

MRI acquisition

High-resolution non-contrast 3D T1-weighted MRI studies were conducted with a 3 Tesla PHILIPS-JSU1335 scanner (Philips Medical Systems, Best, the Netherlands) with 256×256 matrix size, 1 mm slice thickness, 230 to 240 mm field of view, and 9.9 or 7.5 ms repetition time.

Data preprocessing

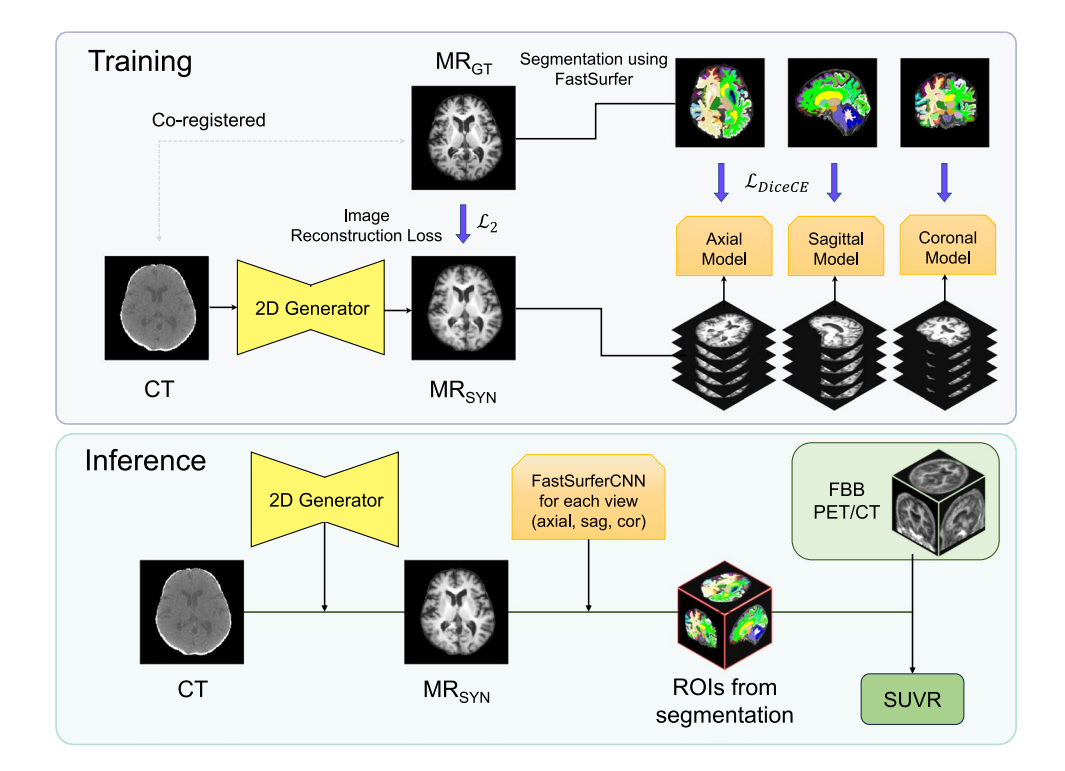
All MR_{GT} and CT images were resampled to voxel sizes of 1 mm \times 1 mm. MR_{GT} and [^{18}F]FBB PET images

were rigidly co-registered to corresponding CT scans using Statistical Parametric Mapping (SPM12), which was executed within MATLAB R2023a, version 9.14 (MathWorks Inc.). Next, segmentation labels for 95 ROIs were obtained from MR $_{\rm GT}$ using FastSurfer [19]. MR $_{\rm GT}$ intensities were robustly cropped at the 99.99th percentile of voxel intensities and rescaled to [0, 1] to remove outlier noise, while CT intensities were clipped between [–100, 200] Hounsfield units (HU) and rescaled to [0, 1] to isolate brain tissue. The resulting MR $_{\rm GT}$ and CT images were skull-stripped using SynthStrip to focus on brain tissue [20].

Study design and automated analysis framework

The pipeline consists of three steps (Fig. 2). First, CT images are translated to MR_{SYN} using a 2.5D residual U-Net implemented in the axial plane, which takes in three-channel input to predict the middle slice. Detailed description of the architecture of the translation network is provided in the Supplementary Fig. 1. Second, the MR_{SYN} is input to three independent 2.5D segmentation networks, which takes in seven consecutive slices to predict the segmentation probability map of the middle slice. Each of the three networks is trained on the axial, sagittal, and coronal views, respectively. To predict the final segmentation mask of 95 classes, the output probability maps from each network are ensembled through weighted average: $p_i = 0.4 * p_{axial,i} + 0.4 * p_{coronal,i} + 0.2 * p_{sagittal,i}$ where p_i indicates the probability of the voxel belonging to the class

Fig. 2 (Top) training scheme, and (bottom) pipeline of the proposed automated analysis framework. In our pipeline, a 2.5D generator is used to translate CT images to synthetic MR images (MR_{SYN}). Then, MR_{SYN} is input to three independent segmentation networks in the axial, coronal, and sagittal planes to predict the segmentation mask, which is applied to PET/CT images to calculate the standardised uptake value ratio (SUVr), L2 loss was used to train the translation network, while weighted cross-entropy and dice loss was used to train the segmentation network. Ground truth MR images (MRGT) and CT images were skull-stripped due to high reconstruction error in the skull regions, which aggravated the translation performance





i. The network architecture is illustrated in Fig. 3. Lastly, the segmentation masks are applied to co-registered PET/CT images to analyse SUVr in ROIs.

The training of the network comprised two stages. First, the translation network was trained by minimizing L2 loss with Adam optimiser (betas = 0.5, 0.999) for 250 epochs; the initial learning rate was set to 10^{-4} , and the batch size was 16. The segmentation networks were trained by minimising weighted cross-entropy and Dice loss with Adam optimizer (betas = 0.9, 0.999) for 50 epochs. The initial learning rate was set to 0.01, which decreased by 70% every 5 epochs, the batch size to 16, and the weight decay to 5×10^{-4} . During training, the number of segmentation labels is reduced from 95 to 78 to merge cortical regions that are adjacent across hemispheres, which simplifies the training process by reducing the number of distinct labels. The original 95-class segmentation map is restored by reassigning the merged labels to their respective hemispheres based on their proximity to the white matter centroids in each hemisphere [19]. All networks were implemented in PyTorch (version 2.0.1) and trained with two NVIDIA RTX A6000 GPUs.

Quantitative evaluation

Each step in the pipeline was evaluated with appropriate metrics. First, normalised root mean squared error (NRMSE), peak signal-to-noise ratio (PSNR), and structural similarity index measure (SSIM) were calculated to quantify similarity between MR_{GT} and MR_{SYN}. Second, Dice similarity coefficient (DSC) was calculated for ROIs between MR_{GT} and MR_{SYN}, where the DSC of region *i* is given by.

$$DSC_i = \frac{2|ROI_{i,GT} \cap ROI_{i,SYN}|}{|ROI_{i,GT}| + |ROI_{i,SYN}|}.$$

The mean DSC scores of all 95 regions (62 cortical regions and 33 sub-cortical structures) were calculated. Subsequently, three representative cases with the lowest, median, and highest DSC were selected to illustrate the quality of MR_{SYN} . A brain surface plot featuring NRMSE and DSC of the cortical structure and the limbic system was illustrated to visualise the correlation between the translation performance (i.e., CT-to- MR_{SYN}) and segmentation performance (i.e., MR_{SYN} -to-ROIs).

Third, the regional and composite SUVr of [¹⁸F]FBB images was measured in the ROIs of the frontal, parietal, lateral temporal, anterior cingulate, posterior cingulate, precuneus, and whole cerebellum in the independent test set, following the common ROIs in the amyloid PET radiotracer. The regional and composite SUVr values were calculated as follows:

$$Regional\ SUVr = \frac{\text{mean counts of ROI}}{\text{mean counts of whole cerebellum}},$$

$$Composite\ SUVr = \frac{\text{mean counts of all ROIs}}{\text{mean counts of whole cerebellum}}$$

Statistical analysis

A Bland–Altman plot was used to assess the agreement of regional and composite SUVr values calculated using ROIs derived from MR_{GT} and MR_{SYN}. Wilcoxon signed-rank test was used to compare the mean difference of regional and composite SUVr between MR_{GT} and MR_{SYN}. All statistical analyses were performed using IBM SPSS for Windows 26.0



(IBM Corp., Armonk, NY, USA). P < 0.05 was considered statistically significant.

Results

Compared to MR_{GT} , the mean NRMSE, PSNR, and SSIM of MR_{SYN} were 0.206 ± 0.072 (mean \pm SD), 30.23 ± 1.64 , and 0.974 ± 0.005 , respectively, demonstrating high similarity between MR_{GT} and MR_{SYN} . Figure 4 illustrates overall quality of segmentation results from three representative cases. Compared to the ROIs of MR_{GT} , the mean and standard deviation of DSC scores of all 95 regions, 62 cortical regions, and 33 sub-cortical structures of MR_{SYN}

were 0.733 ± 0.090 , 0.691 ± 0.054 , and 0.808 ± 0.092 , respectively. All cortical regions had mean DSC greater than 0.600 except cuneus (left hemisphere: DSC = 0.590, right hemisphere: DSC = 0.598), lingual (left hemisphere: DSC = 0.595), right hemisphere: DSC = 0.590), and pericalcarine (left hemisphere: DSC = 0.541, right hemisphere: DSC = 0.552). Meanwhile, substantial agreement of segmentation was observed in the subcortical structures, such as ventricle, basal ganglia, and brainstem. Relatively weaker agreement was observed in the cortical regions, especially in the occipital lobe and the temporal lobe.

The NRMSE and DSC of the cortical structure was visualised in Fig. 5. Regions that exhibited low NRMSE (i.e., high similarity between MR_{GT} and MR_{SYN}) also

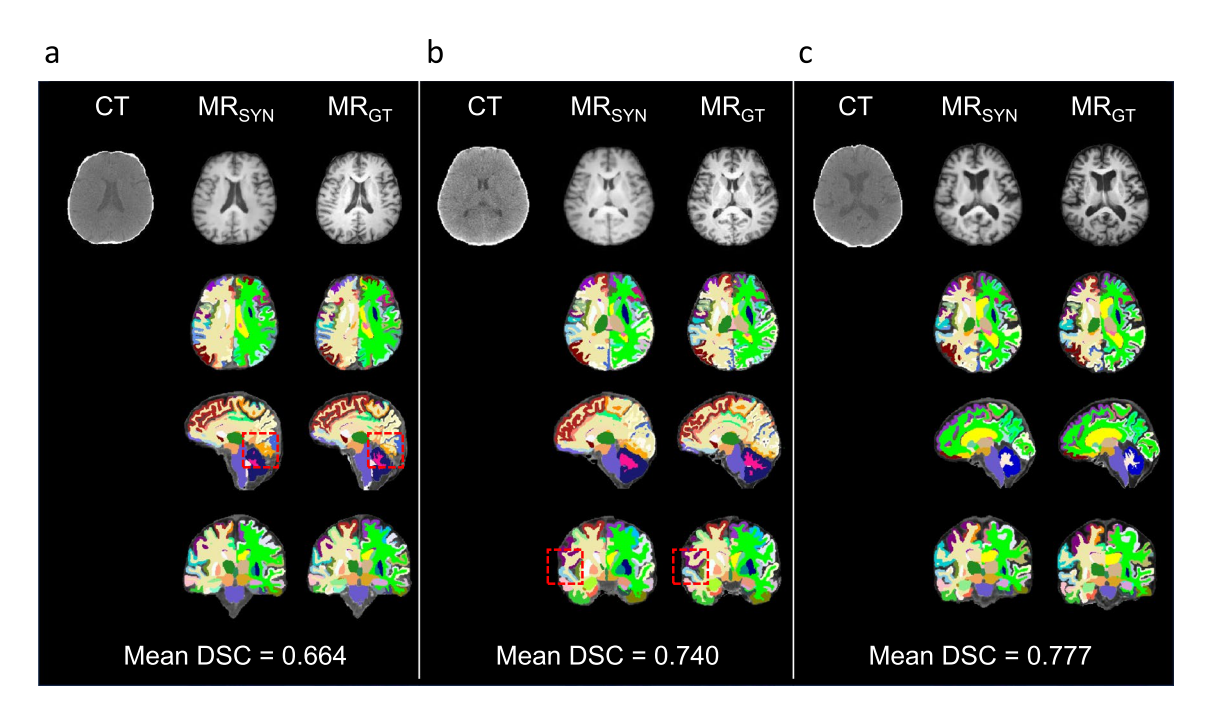
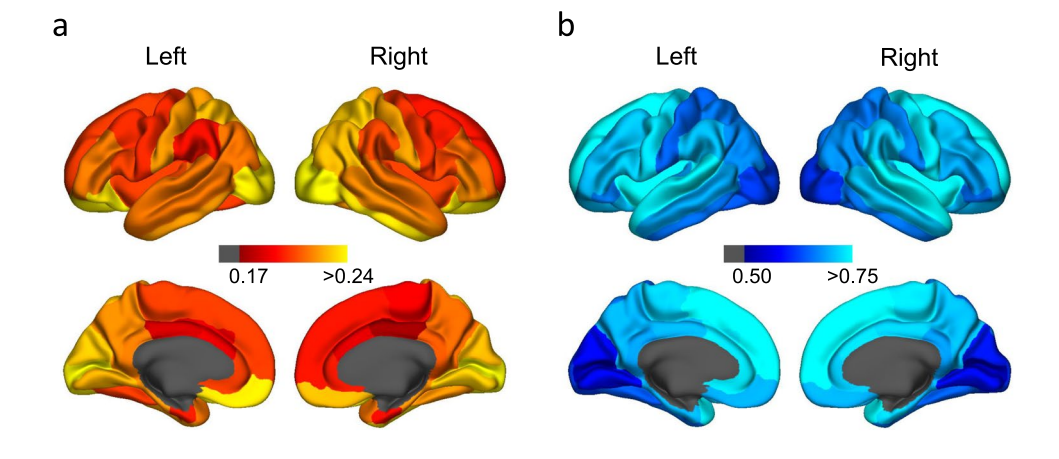


Fig. 4 Visualisation of CT, MR_{SYN} , MR_{GT} , and the segmentation masks in the test set. Three cases with the lowest (a), median (b), and highest (c) mean DSC score are showcased. Dotted squares indicate ROIs with weak agreement

Fig. 5 Visualised quantitative assessment of model performance for CT-to-MR translation and segmentation. In the left, mean NRMSE for each region was calculated between MR_{GT} and MR_{SYN}, where red indicates low NRMSE (a). In the right, mean DSC for each region was calculated between MR_{GT} based segmentation and MR_{SYN} based segmentation, where lighter blue indicates higher DSC (b)





demonstrated high DSC (i.e., high similarity between a ROI derived MR_{GT} and a ROI derived from MR_{SYN}), such as insula (DSC=0.805, NRMSE=0.205) and superior frontal (DSC=0.774, NRMSE=0.200). On the other hand, regions with high NRMSE demonstrated low DSC, such as pericalcarine (DSC=0.533, NRMSE=0.262) and lingual (DSC=0.589, NRMSE=0.229).

The comparison of regional and composite SUVr values between MR_{GT} and MR_{SYN} is summarised in Table 2. No statistical significance was observed in the regional and composite SUVr values except for the precuneus (P=0.001), establishing strong agreement between MR_{GT} and MR_{SYN}-based SUVr measurements. Figure 6 shows the Bland-Altman plots of the regional and composite SUVr values of [18F]FBB images computed with ROIs of MR_{GT} and MR_{SYN}. In the eight sub-figures, the mean differences were close to zero, and 95% of the points lay within the limits of agreement. No systematic pattern was observed in the data. However, one outlier subject exhibited low mean counts of cerebellum in the ROI of MR_{SYN}. Overall, our findings suggest that MR_{SYN}-based SUVr measurement of [¹⁸F]FBB PET/CT can serve as an alternative to MR_{GT}-based measurement.

Discussion

In this retrospective study, we developed a DL-based model to translate CT of PET/CT to MR_{SYN} and evaluated its accuracy quantitatively and qualitatively. Using MR_{SYN} , we developed a DL-based segmentation model for automatic regional analysis. Our proposed analysis framework using MR_{SYN} demonstrated strong agreement with conventional MR_{GT} -based approach (composite SUVr mean difference = 0.003 \pm 0.018). Our results suggest that MR_{SYN}

Table 2 DSC for the ROIs of MR_{GT} and MR_{SYN} , mean SUVr difference, and P-values obtained from the Wilcoxon signed-rank test between SUVr measurement using ROIs of MR_{GT} and MR_{SYN}

		SUVr	
Region	DSC (mean \pm SD)	Difference (mean ± SD)	P
Frontal	0.768 ± 0.035	0.002 ± 0.023	0.711
Parietal	0.722 ± 0.046	0.0 ± 0.019	0.93
Lateral temporal	0.745 ± 0.026	0.005 ± 0.018	0.105
Anterior cingulate	0.747 ± 0.043	-0.003 ± 0.027	0.242
Posterior cingulate	0.713 ± 0.046	-0.001 ± 0.028	1
Precuneus	0.706 ± 0.042	0.016 ± 0.025	0.001
Whole cerebellum ^a	0.943 ± 0.012	3.422 ± 35.499	0.458
Composite	0.763 ± 0.029	0.003 ± 0.018	0.458

a Raw counts are presented instead of SUVr for whole cerebellum because it is used as a reference region



derived from CT images through a DL model can be used to derive ROIs for quantitatively analysing [¹⁸F]FBB PET images when MR images are not available.

Importantly, our approach provides detailed segmentation (95 structured ROIs) in brain PET/CT images with promising segmentation performance (mean DSC \pm SD = 0.733 \pm 0.090), which has not been demonstrated in previous CT-based segmentation approaches due to low soft tissue contrast of CT [16–18]. This detailed segmentation was enabled by leveraging the segmentation labels of MR_SYN that provides high soft tissue contrast. Based on our promising results, our approach can be applied to other brain PET/CT scans such as [18 F]FDG, to provide quantitative analysis without requiring MR images.

The proposed framework achieved strong agreement in composite SUVr (mean difference = 0.003 ± 0.018), indicating that our MR_{SYN}-based approach can serve as an alternative to MR_{GT}-based method for quantifying amyloid load in [18 F]FBB PET/CT scans when MR images are not available. Excluding the precuneus, regional SUVr values exhibited a mean difference less than 0.01, with no statistical significance (P > 0.05). A statistically significant difference in mean SUVr values was found in the precuneus, likely due to the lower DSC in the region, as it is relatively blurry in CT images. Nevertheless, since the precuneus comprises a minor part of the ROIs for measuring amyloid load, its impact on composite SUVr calculations is minimal.

Our framework offers several benefits. First, PET/CT scans can be quantitatively analysed in the absence of MR images. Despite the introduction of PET/MRI years ago, most brain PET examinations are still conducted with PET/CT due to its affordability. Second, CT scans are less affected by metallic implants, which can cause susceptibility artefacts in MR images. Third, since PET images are acquired immediately after the CT scan, the registration between the two images can be readily achieved. This allows for on-the-spot analysis of PET/CT scans, when brain MRI is not accessible. Lastly, the entire analysis framework including both DL-based MR_{SYN} translation and ROI segmentation runs within two minutes per PET/CT scan, providing timely assistance to nuclear medicine physicians in reading PET images.

In this study, a simple L2 norm loss-based U-Net model was adopted to focus on developing an automated analysis framework. This decision was based on the observation that the level of blurring in the MR_{SYN} did not substantially affect the accuracy of downstream segmentation or the subsequent quantitative analysis. Moreover, as PET images exhibit inherently low spatial resolution, the sharpness of the MR_{SYN} may be less critical in this context. However, we acknowledge that recent state-of-the-art (SOTA) methods for image translation such as diffusion models can potentially reduce the blurring, which could enhance the accuracy of segmentation [21]. Future work will address the

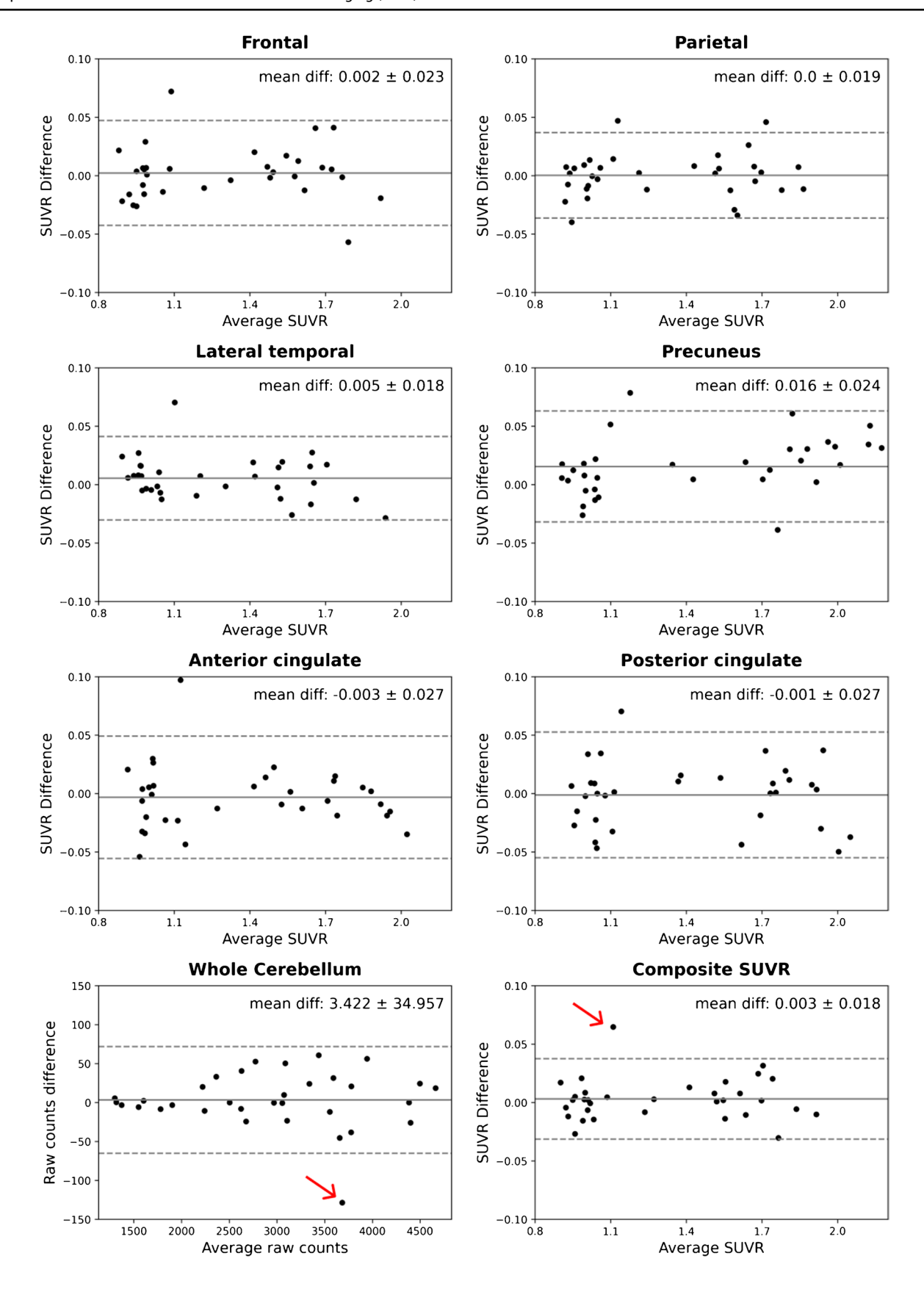


Fig. 6 Bland-Altman plot of composite and regional SUVr values across all test sets. The solid and dashed lines indicate the mean and two standard deviations from the mean, respectively. The red arrows indicate an outlier subject



impact of incorporating SOTA methods into the CT-to-MR translation pipeline.

A few limitations are associated with our technique. First, several ROIs exhibited relatively low DSC, such as pericalcarine (left hemisphere mean DSC=0.541, right hemisphere mean DSC = 0.552). However, these regions are likely attributed to the low detail encapsulated by dense skulls in brain CT. To mitigate this issue, the utilisation of diagnostic CT or photon-counting CT may improve the accuracy of visualising those regions and corresponding translation/segmentation. Second, the overestimation of amyloid burden may occur in patients with cerebellar infarction. We observed that the MR_{SYN}-based ROI included cerebellar infarction in the outlier subject, resulting in low mean counts of the whole cerebellum, as visualised in Supplementary Fig. 2. To overcome this problem, cases with infarction should be collected for training of the network. Lastly, our translation model was implemented in 2.5D, which introduces inter-slice inconsistencies that are visible in the other two planes (i.e., sagittal and coronal). However, our design of the segmentation network mitigates the inconsistencies by aggregating the probability maps of the three views. The generation results and segmentation map from the two other planes are illustrated in Supplementary Fig. 3.

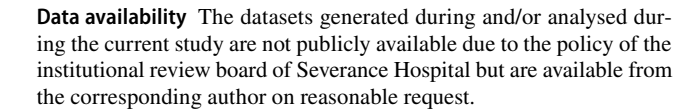
Conclusion

In this study, we developed a deep learning framework for accurate quantification of brain PET in PET/CT. Our findings demonstrate that CT of PET/CT can be translated to MR_{SYN} images to perform MR_{SYN}-based regional segmentation for the quantification of amyloid load in [¹⁸F]FBB PET/CT. Our proposed framework can benefit patients who have difficulties in performing MRI scan.

Supplementary Information The online version contains supplementary material available at https://doi.org/10.1007/s00259-025-07132-2.

Author contributions All authors contributed to the study conception and design. Seongjin Kang performed the collection of PET/CT and MRI studies. Daesung Kim and Kyobin Choo performed data processing and deep learning implementations. Daesung Kim performed experiments, analysed the data, and drafted the manuscript. All authors commented on previous versions of the manuscript. All authors read and approved the final manuscript.

Funding This research was supported by a grant of the Korea Dementia Research Project through the Korea Dementia Research Centre (KDRC), funded by the Ministry of Health & Welfare and Ministry of Science and ICT, Republic of Korea (grant number: RS-2022-KH127174), the Technology Development Program (RS-2024-00467478 and RS-2024-00508913) funded by the Ministry of SMEs and Startups (MSS, Korea), and Basic Science Research Program through the National Research Foundation of Korea (NRF) funded by the Ministry of Education (RS-2024-00465306).



Declarations

Ethics approval All procedures performed in studies involving human participants were in accordance with the ethical standards of the institutional and/or national research committee and with the 1964 Helsinki Declaration and its later amendments or comparable ethical standards. This study was approved by the institutional review board of Severance Hospital (IRB no. 2024–2026-002).

Consent to participate Given the retrospective nature of the study, informed consent was waived.

Consent to publish Consent to publish has been received from all participants.

Competing interests The authors declare no conflict of interest.

References

- Jack CR Jr, Bennett DA, Blennow K, Carrillo MC, Dunn B, Haeberlein SB, et al. NIA-AA research framework: toward a biological definition of Alzheimer's disease. Alzheimers Dement. 2018;14:535–62. https://doi.org/10.1016/j.jalz.2018.02.018.
- Sabri O, Sabbagh MN, Seibyl J, Barthel H, Akatsu H, Ouchi Y, et al. Florbetaben PET imaging to detect amyloid beta plaques in Alzheimer's disease: Phase 3 study. Alzheimers Dement. 2015;11:964–74. https://doi.org/10.1016/j.jalz.2015.02.004.
- Yamane T, Ishii K, Sakata M, Ikari Y, Nishio T, Ishii K, et al. Inter-rater variability of visual interpretation and comparison with quantitative evaluation of 11C-PiB PET amyloid images of the Japanese Alzheimer's Disease Neuroimaging Initiative (J-ADNI) multicenter study. Eur J Nucl Med Mol Imaging. 2017;44:850–7. https://doi.org/10.1007/s00259-016-3591-2.
- Pemberton HG, Collij LE, Heeman F, Bollack A, Shekari M, Salvadó G, et al. Quantification of amyloid PET for future clinical use: a state-of-the-art review. Eur J Nucl Med Mol Imaging. 2022;49:3508–28. https://doi.org/10.1007/s00259-022-05784-y.
- Klunk WE, Koeppe RA, Price JC, Benzinger TL, Devous MD Sr, Jagust WJ, et al. The Centiloid Project: Standardizing quantitative amyloid plaque estimation by PET. Alzheimers Dement. 2015;11:1-15.e4. https://doi.org/10.1016/j.jalz.2014.07.003.
- Della Rosa PA, Cerami C, Gallivanone F, Prestia A, Caroli A, Castiglioni I, et al. A standardized [18F]-FDG-PET template for spatial normalization in statistical parametric mapping of dementia. Neuroinformatics. 2014;12:575–93. https://doi.org/10.1007/ s12021-014-9235-4.
- Kang SK, Heo M, Chung JY, Kim D, Shin SA, Choi H, et al. Clinical performance evaluation of an artificial intelligence-powered amyloid brain pet quantification method. Nucl Med Mol Imaging. 2024;58:246–54. https://doi.org/10.1007/s13139-024-00861-6.
- Seo SY, Oh JS, Chung J, Kim S-Y, Kim JS. MR template-based individual brain PET volumes-of-interest generation neither using MR nor using spatial normalization. Nucl Med Mol Imaging. 2023;57:73–85. https://doi.org/10.1007/s13139-022-00772-4.
- Edison P, Carter SF, Rinne JO, Gelosa G, Herholz K, Nordberg A, et al. Comparison of MRI based and PET template based approaches in the quantitative analysis of amyloid imaging with



- PIB-PET. Neuroimage. 2013;70:423–33. https://doi.org/10.1016/j.neuroimage.2012.12.014.
- 10 Fischl B. FreeSurfer. NeuroImage. 2012;62:774–81. https://doi. org/10.1016/j.neuroimage.2012.01.021.
- Su Y, D'Angelo GM, Vlassenko AG, Zhou G, Snyder AZ, Marcus DS, et al. Quantitative Analysis of PiB-PET with FreeSurfer ROIs. PLoS ONE. 2013;8:e73377. https://doi.org/10.1371/journal.pone. 0073377.
- Klein G, Sampat M, Staewen D, Scott D, Suhy J. P1–035: Comparative assessment of SUVR methods and reference regions in amyloid PET studies. Alzheimer's Dementia. 2015;11:P350-P. https://doi.org/10.1016/j.jalz.2015.06.231.
- Markiewicz PJ, Matthews JC, Ashburner J, Cash DM, Thomas DL, De Vita E, et al. Uncertainty analysis of MR-PET image registration for precision neuro-PET imaging. Neuroimage. 2021;232:117821. https://doi.org/10.1016/j.neuroimage.2021.117821.
- Stadler A, Schima W, Ba-Ssalamah A, Kettenbach J, Eisenhuber E. Artifacts in body MR imaging: their appearance and how to eliminate them. Eur Radiol. 2007;17:1242–55. https://doi.org/10. 1007/s00330-006-0470-4.
- Segovia F, Sánchez-Vañó R, Górriz JM, Ramírez J, Sopena-Novales P, TestartDardel N, et al. Using CT Data to Improve the Quantitative Analysis of 18F-FBB PET Neuroimages. Front Aging Neurosci. 2018;10:158.
- Wang T, Xing H, Li Y, Wang S, Liu L, Li F, Jing H. Deep learning-based automated segmentation of eight brain anatomical regions using head CT images in PET/CT. BMC Med Imaging. 2022;22:99. https://doi.org/10.1186/s12880-022-00807-4.
- Cai JC, Akkus Z, Philbrick KA, Boonrod A, Hoodeshenas S, Weston AD, et al. Fully automated segmentation of head

- CT neuroanatomy using deep learning. Radiol: Artif Intell. 2020;2:e190183. https://doi.org/10.1148/ryai.2020190183.
- Han T, Wang H. Gray and White Matters Segmentation in Brain CT Images Using Multi-task Learning from Paired CT and MR Images. International Workshop on New Approaches for Multidimensional Signal Processing: Springer; 2023. p. 181–90.
- Henschel L, Conjeti S, Estrada S, Diers K, Fischl B, Reuter M. FastSurfer - A fast and accurate deep learning based neuroimaging pipeline. Neuroimage. 2020;219:117012. https://doi.org/10.1016/j.neuroimage.2020.117012.
- Hoopes A, Mora JS, Dalca AV, Fischl B, Hoffmann M. Synth-Strip: skull-stripping for any brain image. Neuroimage. 2022;260:119474. https://doi.org/10.1016/j.neuroimage.2022. 119474.
- Choo K, Jun Y, Yun M, Hwang SJ. Slice-Consistent 3D Volumetric Brain CT-to-MRI Translation with 2D Brownian Bridge Diffusion Model. In: Linguraru MG, Dou Q, Feragen A, Giannarou S, Glocker B, Lekadir K, Schnabel JA, editors. Medical Image Computing and Computer Assisted Intervention MICCAI 2024. Cham: Springer Nature Switzerland; 2024. p. 657–67.

Publisher's Note Springer Nature remains neutral with regard to jurisdictional claims in published maps and institutional affiliations.

Springer Nature or its licensor (e.g. a society or other partner) holds exclusive rights to this article under a publishing agreement with the author(s) or other rightsholder(s); author self-archiving of the accepted manuscript version of this article is solely governed by the terms of such publishing agreement and applicable law.

